

# Study and Applications of Dynamic Resistance Profiles During Resistance Spot Welding of Coated Hot-Stamping Steels



OSAYANDE LORD-RUFUS IGHODARO, ELLIOT BIRO, and Y. NORMAN ZHOU

This work compares the role of press hardened steel coating type (Al-Si and GA) on resistance spot welding by analyzing the dynamic resistance curves measured during the weld cycles of the respective materials. It was seen that the dynamic resistance profiles for GA- and Al-Si-coated steels are similar. But the GA specimens exhibited higher resistance than Al-Si-coated specimens in the as-received condition, while the Al-Si-coated specimens exhibited higher resistance after hot stamping. From the early stages of the dynamic resistance profiles, data were obtained and applied for computing the values of components of resistances associated with the different coatings since each coating exhibits characteristic value at the early stages. The results revealed that at the start of the welding cycle, the resistance of the electrode/sheet interface was significantly higher than that of the faying surface or the bulk resistance regardless of whether the steel was Al-Si- or GA-coated. The possible uses of these resistance values in studying welding current requirement and electrode tip life were discussed.

DOI: 10.1007/s11661-016-3899-3

© The Minerals, Metals & Materials Society and ASM International 2016

## I. INTRODUCTION

RESISTANCE spot welding (RSW) is a process of joining two or more metal sheets at discrete spots and is the most common technique employed in joining sheet metal during body-in-white (BIW) assembly of automobiles.<sup>[1,2]</sup> It is based on the Joule heating effect where heat energy is generated by passing an electrical current through the joint over a given period. The heat generated melts the material, forming a nugget at the faying surfaces of the workpieces. The quantity of heat generated ( $Q$ ) can be quantified (neglecting heat losses) by the equation:  $Q = i^2 \cdot R \cdot t$ , where  $i$  is the current,  $R$  is the resistance, and  $t$  is the duration of the current. During the welding process, the electrical resistance of the joint changes, which may be measured during the cycle to reveal a characteristic dynamic resistance profile with respect to a set of parameters and material. Additionally, automotive steel sheets are manufactured with different coatings, which impart characteristic resistance profile during RSW. Thus, dynamic resistance profile may be used to study the process and perform non-destructive evaluation and quality monitoring of RSW process during production.<sup>[3-5]</sup>

Zn coating offers protection against corrosion. Al-Si coating also serves to protect press hardened steels against decarburization and oxidation during hot stamping. These coatings on steel significantly affect RSW parameters and joint properties;<sup>[6-8]</sup> therefore, dynamic resistance profile study of the different coating systems will help foster better understanding and quality monitoring of the joining stage during RSW manufacturing processes. It can also help in the development of coating systems for the enhancement of weldability by RSW process. For example, from dynamic resistance profile the time necessary to remove the coating from the faying surfaces or the change in resistance profile with the change in coating composition may be measured; this information can be used in the development or enhancement of the coating system for specific applications.

Research has been performed on the dynamic resistance of Zn-based coating steels.<sup>[3,9,10]</sup> For example, Gedeon *et al.*<sup>[4]</sup> identified six stages in the dynamic resistance profile for galvanized (GA) steels and four stages for uncoated steels. But no work has been performed on the dynamic resistance profile of Al-Si-coated steel. The research presented in this paper describes the resistance response of Al-Si-coated hot-stamping steel (Usibor®) during RSW process, as compared to galvanized coating on similar substrate steel. The resistances associated with these coatings are also computed and compared.

### A. Technical Background

Figure 1(a) shows a sketch of the set-up for RSW and the various resistances involved.  $R_1$  and  $R_7$  are the resistances of the electrodes,  $R_3$  and  $R_5$  are the bulk

OSAYANDE LORD-RUFUS IGHODARO and Y. NORMAN ZHOU are with the Mechanical and Mechatronics Engineering Department, University of Waterloo, 200 University Avenue West, Waterloo, ON N2L 3G1, Canada. Contact e-mail: olighoda@uwaterloo.ca ELLIOT BIRO is with the Mechanical and Mechatronics Engineering Department, University of Waterloo, and also with ArcelorMittal Global Research, 1390 Burlington Street East, Hamilton, ON L8N 3J5, Canada.

Manuscript submitted January 26, 2016.

Article published online December 20, 2016

resistances of the substrate metal sheets to be welded,  $R_2$  and  $R_6$  are the contact resistances at the electrode/sheet (e/s) interface,  $R_4$  is the contact resistance at the sheet/sheet (s/s) interface, and  $F_E$  is the electrode force. Figure 1(b) shows the coating and oxide film layer on the sheet surface. Whenever two electrical conductors are in connection through an interface, an electrical contact resistance (ECR) exists. ECR results due to asperities on the surfaces of the metals, which allow only a small fraction of the surfaces to be in actual contact, the current flow is constricted through small conducting spots. This gives rise to constriction resistance.<sup>[11]</sup> The force  $F_E$  clamping the surfaces together may be able to deform the contact spots and also make more contacts, increasing the nominal contact area ( $A_n$ ), depending on the hardness of the surface. The relation

$$A_n = F_E / \zeta H \quad [1]$$

is satisfied, where usually  $0.2 < \zeta < 1$  and  $H$  is the contact hardness.<sup>[11]</sup> This shows that the contact area reduces as the contact hardness increases. Thus, harder surfaces exhibit higher constriction resistance. Likewise, higher clamping force increases the contact spots (contact area), causing a reduction in constriction resistance. Another component of contact resistance associated with metallic surfaces is film resistance. Usually, metallic surfaces (unless specially treated and preserved) are covered with surface films, oxide layers, or some contaminants.<sup>[5,12]</sup> This gives rise to some resistance to the flow of current and is termed film resistance. For coated sheets, the coating also has electrical resistance which depends on coating material and thickness; also, the coating surface is usually covered with some contaminants. During RSW of coated steels, constriction, film, and coating resistances are always present together inseparably at the interfaces. Therefore, their effects can be summed up to determine the total resistance at an interface. For the purpose of computation, the resistances are grouped into three major components: electrode/sheet resistance, bulk resistance, and faying interface resistance.

### 1. Electrode/sheet resistance

The electrode/sheet resistance ( $R_{e/s}$ ) is represented in Figure 1(a) as  $R_2$  or  $R_6$ . Its value is governed by the texture and hardness of the surfaces as well as the materials. The value of  $R_{e/s}$  is highest at the beginning of RSW, and as welding progresses, the value diminishes as a result of softening and flattening of asperities due to heating effect, but it never disappears completely. It comprises the film, constriction, and coating resistances, and may be more explicitly written as

$$R_{fi} + R_{cn} + R_{co} = R_{e/s}, \quad [2]$$

where  $R_{fi}$  is the film resistance,  $R_{cn}$  is the constriction resistance, and  $R_{co}$  is the coating resistance, summing to  $R_{e/s}$ —the electrode/sheet resistance.

### 2. Faying interface resistance

The faying interface contact resistance ( $R_{fa}$ ) is essential in RSW because nugget formation takes place at this location. The higher the faying interface contact

resistance, the faster the nugget will form; thus, when faying interface resistance is low, higher current is usually required to form an acceptable nugget (for a given welding time). Faying interface resistance is highest at the commencement of RSW process. It gradually diminishes during heating and finally disappears when melting and nugget formation commence. As shown in Figure 1(a) and (b) (represented as  $R_4$ ), it comprises film, constriction, and coating resistances, and may be expressed as

$$2R_{fi} + 2R_{cn} + 2R_{co} = R_{fa}, \quad [3]$$

where  $R_{fa}$  is the sum of the resistances at the faying surfaces.

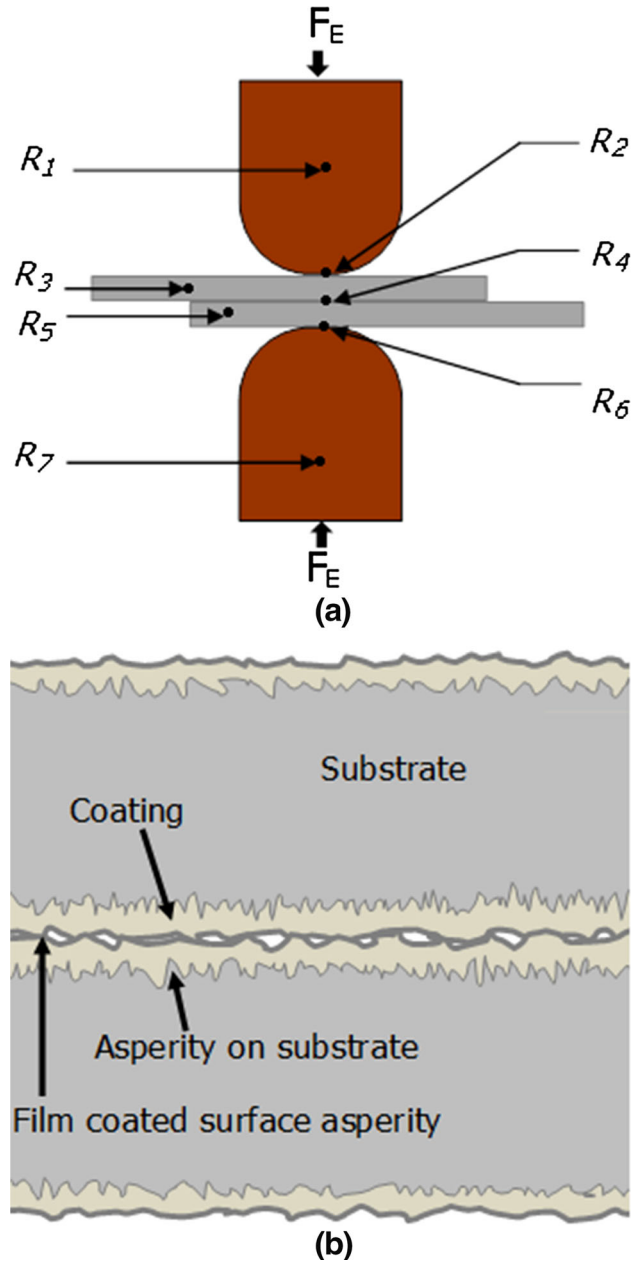


Fig. 1—Resistances encountered in resistance spot welding: (a) set-up and (b) expanded view of stacked sheets showing features on the surfaces of coated substrates.

### 3. Bulk resistance ( $R_b$ )

The bulk resistance, represented as  $R_3$  or  $R_5$  in Figure 1(a), has a defined relationship which can be given as

$$\rho \frac{l}{A} = R_b, \quad [4]$$

where  $\rho$  is the resistivity of the substrate,  $l$  is the length of current path, and  $A$  is the apparent contact area.

### 4. Resistance during welding

From the RSW set-up shown in Figure 1(a), the total resistance ( $R_{T2}$ ) of a 2-stack sheet at any time can be expressed as

$$2R_{Cu} + 2R_{e/s} + 2R_b + R_{fa} = R_{T2} \quad [5]$$

with  $2R_{Cu}$  being the electrode resistance represented as  $R_1$  and  $R_7$ . Now, considering a situation where a single sheet is involved in the set-up as shown in Figure 2, the faying interface is absent, and therefore the total resistance ( $R_{T1}$ ) of the single sheet may be expressed as

$$2R_{Cu} + 2R_{e/s} + R_b = R_{T1}. \quad [6]$$

Subtracting Eq. [6] from Eq. [5] yields

$$R_{fa} + R_b = R_{T2} - R_{T1}. \quad [7]$$

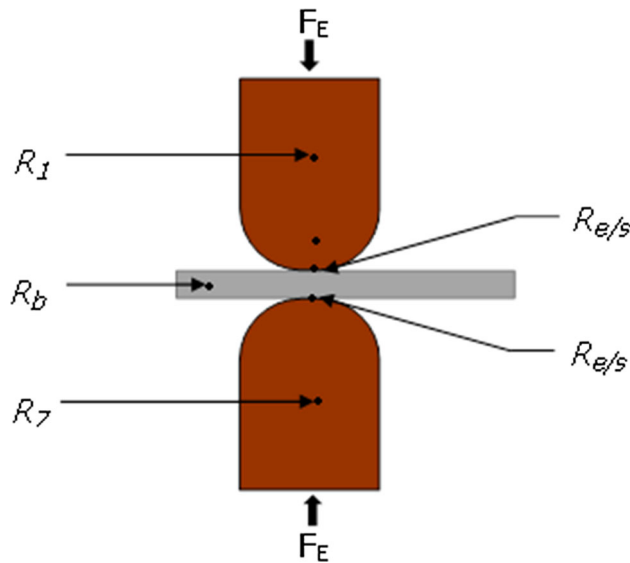


Fig. 2—RSW set-up for a single sheet.

Using Eq. [7], the total resistance at the faying interface,  $R_{fa}$ , can be computed, since  $R_b$  can be computed and both  $R_{T2}$  and  $R_{T1}$  are measurable data.

## II. EXPERIMENTS

### A. Materials

The materials used in this work are Al-Si-coated and galvanized (GA) hot-stamping steels (Usibor<sup>®</sup>), and the nominal sheet thickness is 1.2 mm. Alloying elements for the Al-Si- and GA-coated sheets are given Table I. The materials were investigated in both the as-received and hot-stamped conditions. Hot stamping was done at 1173 K (900 °C) for 6 minutes. All the hot-stamped GA sheets were sandblasted after hot stamping to thoroughly clean the surfaces.

### B. Electrical Resistivity and Resistance Measurements

Resistivity values of the substrates (25 mm by 300 mm) were measured based on the ASTM standard B193-02 using an Agilent 34420A NanoVolt/Micro-Ohm meter after the coatings were removed. The GA coating on the substrates was removed by soaking them in a solution of HCl (mixture ratio of HCl:H<sub>2</sub>O was 1:3) for about 10 hours when the reaction was observed to have ended. The Al-Si coating was removed by soaking in a solution of NaOH obtained by dissolving 10 g of NaOH in a liter of water. Four measurements were made on the as-received specimens and also the hot-stamped specimens for Al-Si and GA sheets.

Static electrical resistance measurements were made on specimens in the as-received as well as hot-stamped conditions using four-point measuring method according to ISO 18594:2007 (E) standard. The DC power supply used for this measurement was a TEKPOWER 3465A and voltage was measured using an Agilent 34411A multimeter. The clamping force was 4.4 kN. For dynamic resistance, the profiles were recorded by the Genius HWI 516W welder controller.

### C. Welding Process

All welding operations were performed using a 144/180 kVA Mid-Frequency Direct Current (MFDC) Resistance Spot Welder. Welding electrodes were RWMA Group A, Class II, with a domed-flat nose, and a face and a body diameter of 6 and 16 mm, respectively. The specimens were welded in both the as-received and hot-stamped conditions for Al-Si and GA sheets after cleaning with acetone. Other parameters included a weld force of 4.4 kN, single pulse, a hold time of 150 ms, and a cooling water flow rate of 4 L/min. The

Table I. Alloying Compositions of the Al-Si- and GA-Coated Usibor Steels in Weight Percent

Coatings	C	Mn	P	Si	B	Cr	N
Al-Si	0.23	1.22	0.013	0.27	0.0032	0.20	—
GA	0.22	1.17	0.012	0.25	0.0025	0.18	0.0064

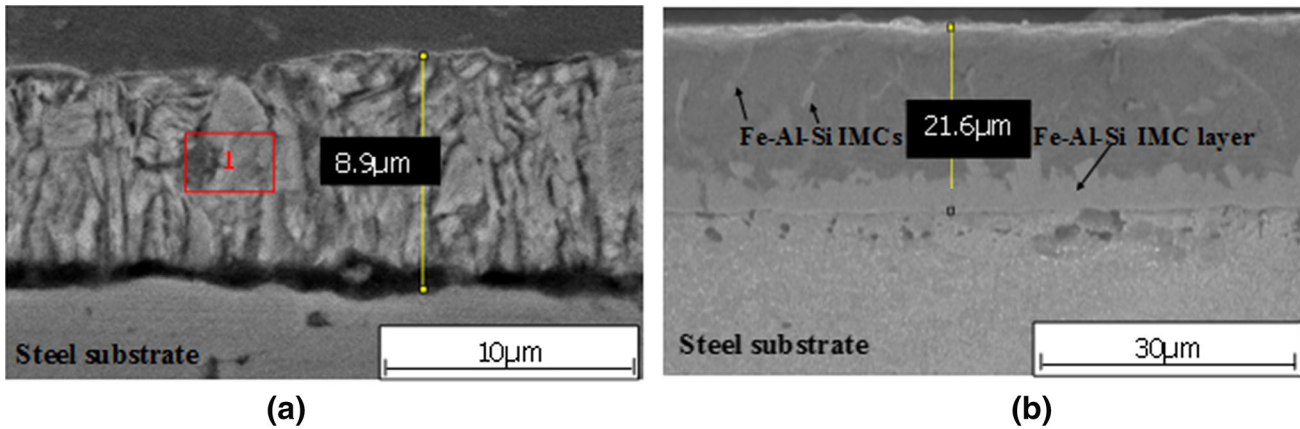


Fig. 3—Coating characteristics in the as-received condition for (a) GA and (b) Al-Si.

weld time was varied to observe different stages during the welding process.

#### D. Metallography and Microstructure

Metallographic sections were prepared for coating thickness measurement and microstructural examinations after etching with nital etching reagent (5 pct nitric acid in 95 pct ethanol). A scanning electron microscope (JEOL JSM 6460) was used for measuring coating thickness and microstructural examinations. Identification of elemental compositions in the coatings was done using EDX (Oxford Instrument Microanalyses System) spectroscope fitted to the electron microscope.

### III. RESULTS AND DISCUSSION

#### A. Coating Characteristics

##### 1. Coatings in the as-received condition (before hot stamping)

Coating characteristics for the as-received materials are shown in Figure 3. From Figure 3(a) the coating thickness for the GA is  $\sim 9 \mu\text{m}$ . EDX analysis conducted on the square area marked “1” reveals 11.9 wt pct Fe and 88.1 wt pct Zn, which indicates predominantly a delta phase region, which is in agreement with the literature.<sup>[1,13]</sup> Figure 3(b) shows the Al-Si-coated specimen, and the coating thickness is  $21.6 \mu\text{m}$ . EDX analysis conducted on the intermetallic phase compounds (IMCs) reveals the elemental compositions (in wt pct) of 61.2, 20.1, and 18.7 for Fe, Al, and Si, respectively. These IMCs consist of different Fe-Al-Si phases formed during the annealing process, depending on the Si content and the coating parameters during hot-dip.<sup>[14–16]</sup>

##### 2. Coatings in hot-stamped condition

Figure 4 shows the microstructure of the coatings after hot stamping at 1173 K (900 °C) for 6 minutes. The changes in the microstructure (compared to Figure 3) are the result of diffusion and interaction between the steel substrate and the coatings. During

heat treatment of Zn-coated steel, Zn diffuses into the steel substrate forming various IMCs in proportions dependent on temperature and time. Fe also diffuses across the interface into the Zn-rich layer but at a much slower rate.<sup>[13,17]</sup> This kinetics increases the coating thickness layer and changes composition after hot stamping, thereby increasing the total resistance of the sheet. Also, hot stamping of Al-Si-coated steel results in phase changes in the coating as well as an increase in coating thickness due to atomic diffusion across the coating/substrate interface.<sup>[14,15,17]</sup> In the work of Windmann *et al.*,<sup>[14]</sup> they showed that Al-Fe-Si IMCs exist in the coating only before austenitization (*i.e.*, in the as-received condition). During austenitization [at about 1173 K (900 °C)] for periods of up to 2 minutes, the Al-Fe-Si phases no longer exist, while for a dwell time of 6 minutes all the phases are converted into phases of types  $\text{Fe}_2\text{Al}_5$  and  $\text{FeAl}$ .<sup>[14,16]</sup> It is therefore expected that the resistances associated with the as-received and hot-stamped materials will be different.

#### B. Resistivity and Resistance Values

##### 1. Resistivity and static resistance

The resistivity values of the substrate in the as-received condition for both Al-Si- and GA-coated specimens are similar, *i.e.*, having a value of  $(23.02 \pm 0.36) \times 10^{-8} \Omega\text{m}$ , without any significant difference, while the resistivity in the hot-stamped condition for both specimens is  $(23.78 \pm 0.45) \times 10^{-8} \Omega\text{m}$  at 95 pct confidence interval.

The results of the 4-point static resistance measurements, which are the total resistance values across the electrodes in a two-sheet stack for RSW, are shown in Figure 5. Observing that the Al-Si- and GA-coated steels have the same bulk resistance value (since their resistivities are similar), any differences in measured total resistance must be associated with the coatings and their surface effects. Pure Al-Si that remains as the major compound in the coating layer of Al-Si-coated specimen (volume fraction of IMCs is relatively low in the as-received coating condition) has room-temperature electrical resistivity between 3.89 and  $4.25 \mu\Omega \text{cm}$  (for the near-eutectic composition).<sup>[18]</sup> Conversely, the

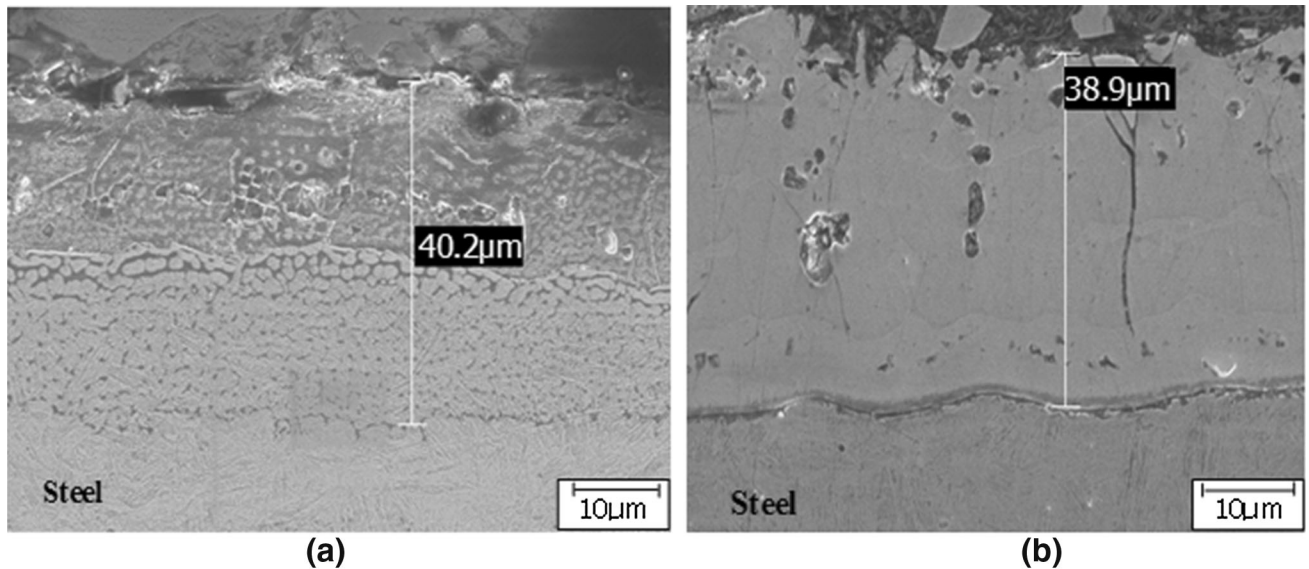


Fig. 4—Coating characteristics in hot-stamped condition for (a) GA and (b) Al-Si.

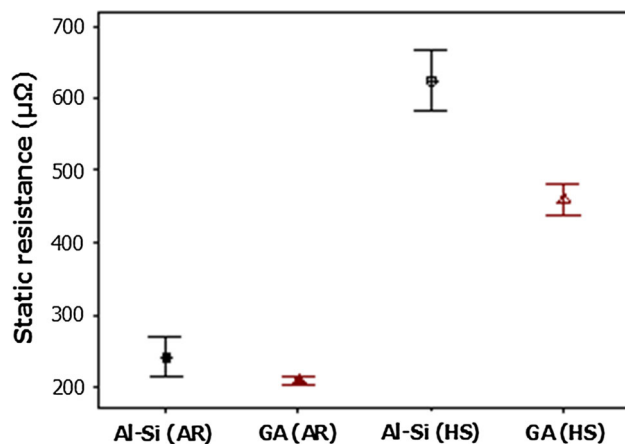


Fig. 5—Static resistance values from 4-point resistance measurements.

delta phase which is the major component in the GA-coated steel has a room-temperature resistivity of  $331 \mu\Omega \text{ cm}$ .<sup>[19]</sup> However, in the as-received condition, as shown in Figure 5, the total resistance for Al-Si (AR) is higher than the resistance for GA (AR) despite the much higher value of resistivity of the GA coating (although the coating thickness of Al-Si (AR) is about 2.4 times that of GA (AR) as shown in Figure 3). This difference in the static resistances of materials is due to differences in their contact resistances, which is due to the resistances of the oxide and the constriction resistances of the different coatings. It should be noted that Al-rich materials usually develop a thin film of  $\text{Al}_2\text{O}_3$  on the surface.<sup>[14]</sup> The  $\text{Al}_2\text{O}_3$  layer having a very high electrical resistance would contribute significantly to the measured static resistance of the Al-Si (AR) specimen, boosting its value above the resistance value of GA (AR).

During hot stamping of the GA-coated material, austenitization at 1173 K (900 °C) transformed all the

intermetallic phases to the liquid phase and Fe-Zn solid solution since no intermetallic exists above 1055 K (782 °C) as observed from the Zn-rich end of the Fe-Zn phase diagram shown in Figure 6. After quenching from the austenitization temperature to room temperature, various Fe-Zn intermetallics and solid solution are formed, but because the quenching process is not at equilibrium it is not certain what fractions of the different phases are present in the hot-stamped coating. However, since the as-received GA also consists of similar phases (possibly in different proportions), the higher resistance exhibited by the hot-stamped GA can largely be accounted for by the growth of the coating layer as a result of hot stamping. From Figure 5, it can also be observed that the Al-Si (HS) exhibits significantly higher resistance than the GA (HS) specimen: As expected, firstly, the phases present in the Al-Si (HS) specimen showed high resistivity.<sup>[20–22]</sup> Secondly, during high-temperature austenitization, the formation of  $\text{Al}_2\text{O}_3$  surface oxide film thickness also increases due to higher oxidation activity, resulting in the observed higher electrical resistance values. To summarize, all hot-stamped specimens possess higher resistance values than the specimens in the as-received conditions and this could be due to (a) the formation of compounds having higher resistances than the as-received coatings (as in the case of Al-Si), (b) the growth of coating thickness, (c) the rougher and harder surfaces, and (d) the thicker surface oxide film after hot stamping. However, static resistance is of little significance as regards weldability because once current passes through the contact points and welding commences, heating of the workpieces begins, causing changes in properties (especially along the current path, between the electrodes). Thus, contact resistance begins to change continuously during the welding process, leading to the generation of dynamic resistance as will be shown later. Therefore, dynamic resistance values are better indicators of the characteristics and influence of coating on RSW process.

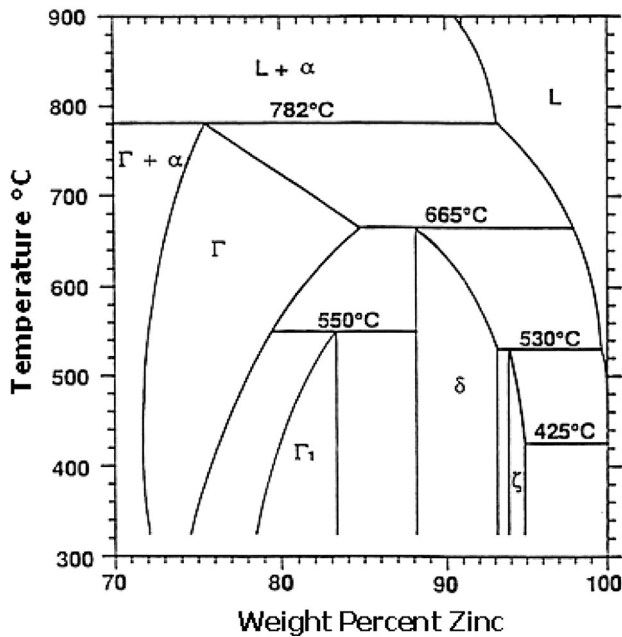


Fig. 6—Zinc-rich corner of Fe-Zn binary phase diagram.<sup>[13]</sup>

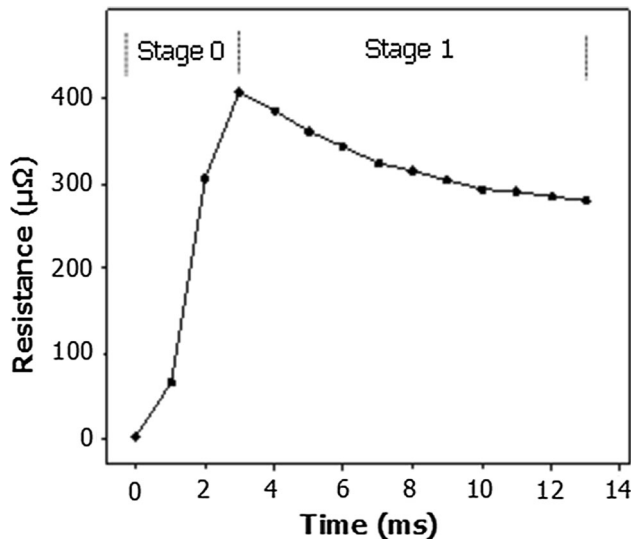


Fig. 7—Stages 0 and 1 of the dynamic resistance profile for Al-Si (HS), using 7.5 kA current, for the first 13 ms, showing rise to a peak followed by a sharp drop in resistance.

## 2. Dynamic resistance stages for Al-Si-coated steel in the hot-stamped condition

The stages encountered in the dynamic resistance profiles generated between the electrodes (*i.e.*, electrode-to-electrode profile) for hot-stamped Al-Si-coated steels are first presented in this section. This is mostly based on the model presented by Gedeon and Eager<sup>[9]</sup> for galvanized steel, but a new stage “0” has been added.

**Stage 0 (Surface heating)** Figure 7 shows this stage on the dynamic resistance profile for hot-stamped Al-Si, using 7.5 kA welding current. This rising profile exists before the peak, before the sharp drop of stage 1 began,

which is missed from the model by Gedeon and Eager.<sup>[9]</sup> Tan *et al.*<sup>[23]</sup> observed this stage during small-scale RSW of Ni sheets. This will be discussed in depth in a later section after the existing model is described.

**Stage 1 (Surface film breakdown)** This stage is characterized by a sharp drop in resistance due partly to fritting, a complex process of oxide film insulation breakdown,<sup>[3,5,9,23]</sup> and partly to some asperity collapse, making the drop in resistance more pronounced. During this stage, heating is concentrated in the surface oxide film layer because no appreciable current flows through, and the sheet stack remains at room temperature to the end of stage 1.<sup>[5,9]</sup> The end of stage 1 marks the end of the effect of surface oxide film layer. Figure 8 shows the microstructure at the end of stage 1 (13 ms).

**Stage 2 (Heating and softening of the coating)** During this stage, heating is concentrated on the coating at the faying and e/s interfaces. Some bulk heating also takes place, resulting in a rise in the dynamic resistance profile. The major microstructural feature of this stage is pronounced collapsing of asperities due to softening of the coating as the temperature increases. Figure 9 shows the resistance profile up to the end of stage 2 for hot-stamped Al-Si. The microstructure shows the image at the faying interface at 20 ms (*i.e.*, end of stage 2). Asperity flattening at the faying interface is more pronounced compared to stage 1 (shown in Figure 8). Also, flattening of asperities is more pronounced at the faying interface than the e/s interfaces due to lower temperature around the electrodes. Flattening of asperities causes a reduction in resistance, but heating of the coating and bulk material causes resistance to rise, resulting in a net rise in dynamic resistance profile.

**Stage 3 (Coating melts)** As heating and softening continue beyond stage 2, eventually the coating begins to melt (especially at the faying interfaces). The microstructure at the beginning of this stage (which is also the interface between stages 2 and 3) is shown in Figure 10(b). As the coating melts, it spreads, increasing the area of contact, causing a decline in resistance. Also, electrode pressure squeezes the molten coating away from under the electrodes as the bulk sheets move closer, reducing the current flow path; this also causes a reduction in resistance. Eventually, net resistance peaks and begins to decline shortly after coating begins to melt. Figure 10(a) shows the dynamic resistance profile for Al-Si (HS) up to 31 ms (end of stage 3). Figure 10(c) shows the microstructure of a faying interface corresponding to 31 ms of weld time at 7.5 kA. It shows that the molten coating is displaced (from under the electrode).

**Stage 4 (Bulk heating/melting)** After the coating is displaced from the faying interfaces, heating is now concentrated on the bulk steel substrate. The resulting sheet/sheet (s/s) interface resistance and increase in bulk resistance due to an increase in resistivity with temperature cause resistance to increase. However, increase in temperature causes increased softening of coating. Consequently, the electrodes dip into the coating at the e/s interfaces and more coating is displaced from the faying interface. These events reduce the current path and increase the contact area, causing resistance to

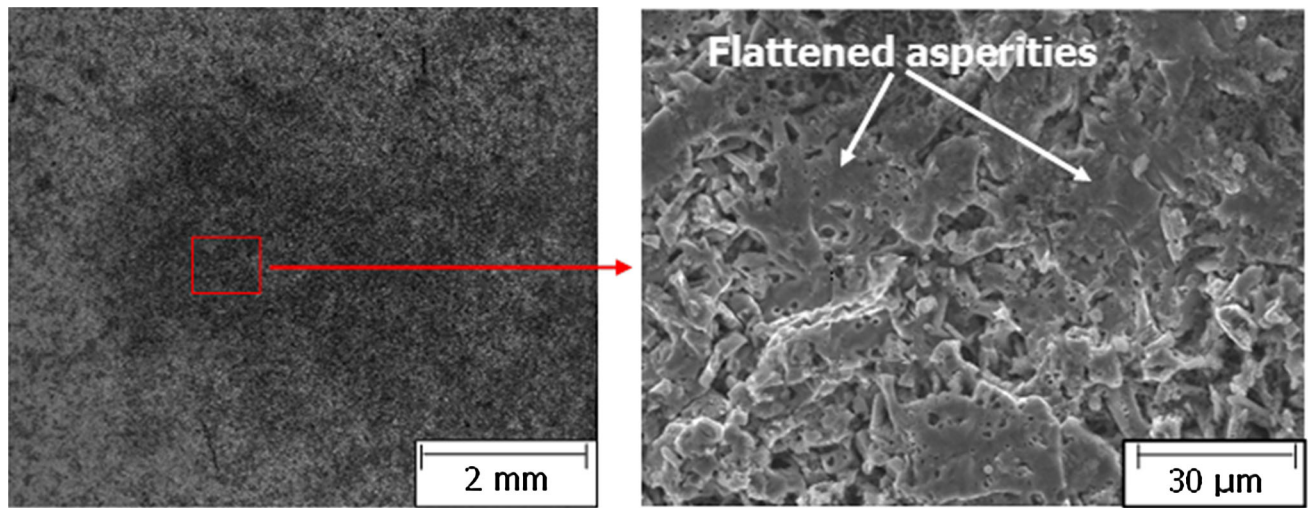


Fig. 8—A faying interface of Al-Si (HS), 7.5 kA current, after 13 ms, showing some flattened asperities. This corresponds with the end of stage 1.

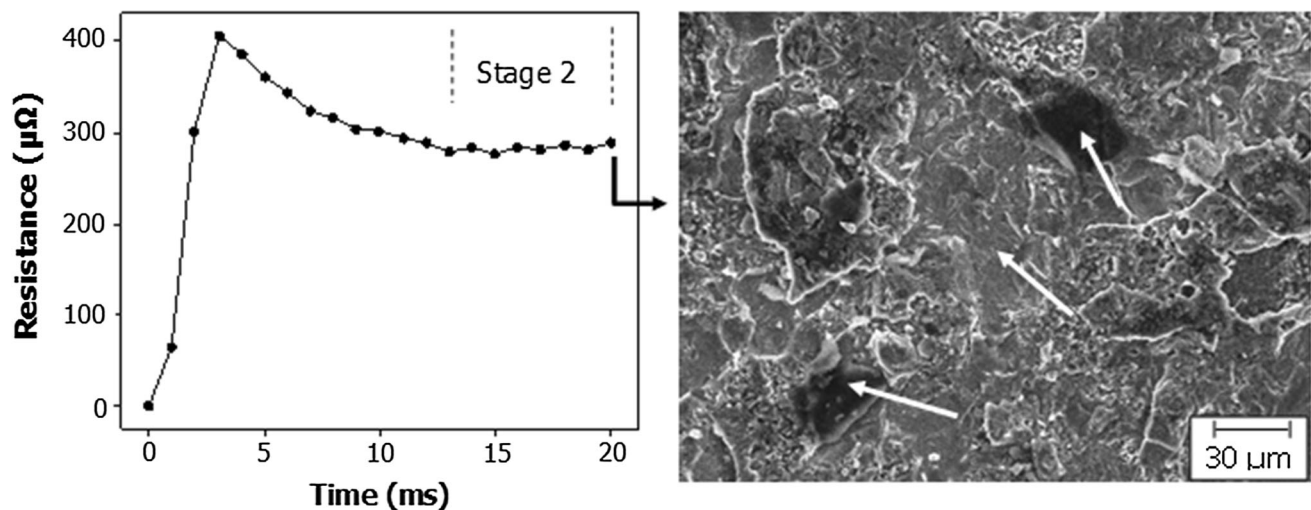


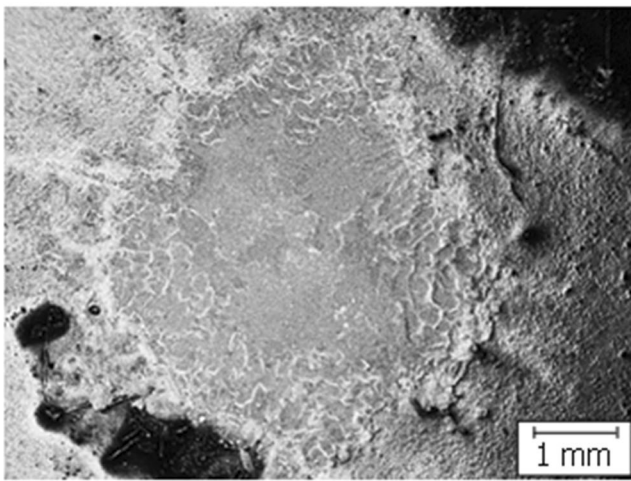
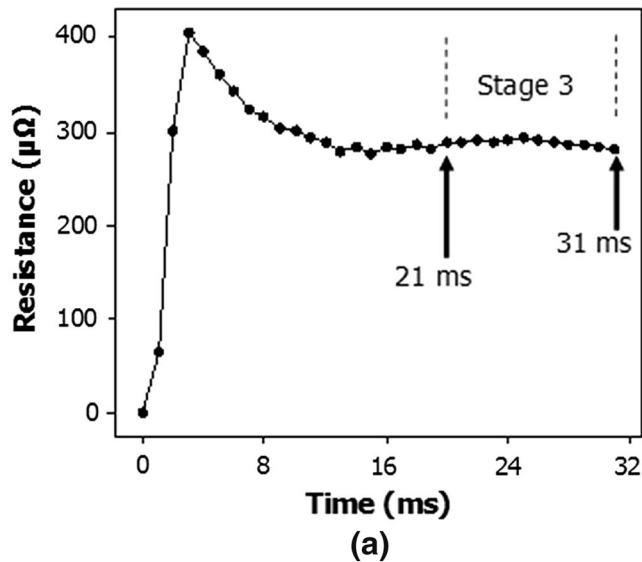
Fig. 9—Stage 2, rising portion of the resistance profile due to heating of Al-Si (HS) coating, weld current 7.5 kA, and microstructure of a faying interface, at 20 ms (end of stage 2), showing pronounced flattening of asperities (arrows) due to softening of the coating.

reduce. Increasing temperature with time also causes more asperity flattening at the e/s interface, contributing to the lowering of resistance. Figure 11(b) shows an image of a faying interface with substrate steel being exposed after 46 ms of welding. As the heating of bulk sheets continues, another phase change (melting), the commencement of nugget formation, begins, as shown in Figure 11(c). Nugget formation causes the (gradual) elimination of faying interface resistance, contributing also to a reduction in resistance. But melting causes an increase in resistance of steel due to an increase in resistivity with melting.<sup>[24]</sup> A significant increase in resistance associated with heating and melting of steel during stage 4 should appear as a hump on the dynamic resistance profile.<sup>[3,9,23]</sup> But due to the opposing directions of resistance components the hump may not be obvious in the dynamic resistance profile; this is the situation in Figure 11(a).

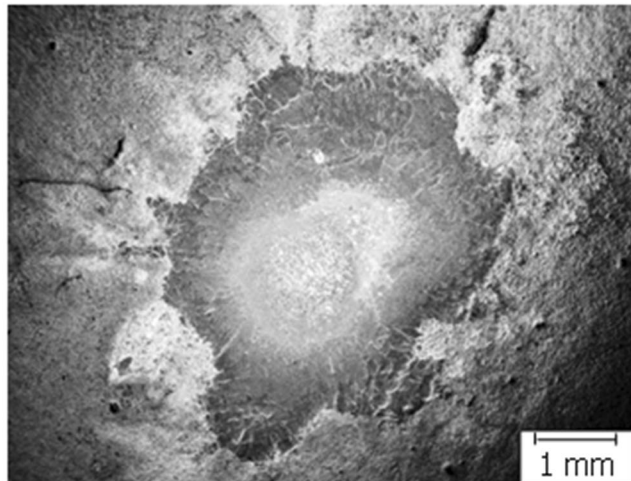
*Stage 5 (Nugget growth)* Shortly after the commencement of melting and nugget progresses in size, a

significant volume of molten metal now exists. This causes mechanical breakdown and electrode close-up movement, which results in indentation and reduction of current flow path. Also the contact area increases as the nugget grows. These effects cause the resistance profile to peak and begin a downward trend as shown in Figure 12.

*Stage 6 (Expulsion)* This stage is undesirable but for completeness it is included. Expulsion stage may be reached if heating continues and nugget growth continues to a size when the molten metal pressure can no longer be contained under the electrode pressure. This situation can be caused by excessive current or time and leads to the expulsion of molten metal. It is characterized by a sudden drop in resistance during the nugget growth stage. It also shows up as severe indentation on the welded joint. Expulsion will also occur if the current is excessive. In this case, the nugget will not necessarily grow to optimal size before expulsion occurs. This is because the very high heating rate creates a localized



(b)



(c)

Fig. 10—(a) Dynamic resistance profile for Al-Si (HS) at 7.5 kA weld current showing the peak and subsequent decline as the coating melts and is displaced in stage 3; (b) microstructure of faying interface at the beginning of stage 3 (21 ms), showing molten coating; (c) microstructure corresponding to the end of stage 3 (31 ms), showing that the coating is displaced.

high pressure which causes expulsion. Expulsion is generally undesirable because of loss of material and consequent loss of strength of the joint. Figure 12 also includes stage 6, showing a nugget exhibiting expulsion due to excessive weld time.

After experimentation with Al-Si-coated specimens in hot-stamped conditions, similar experiments were also conducted for Al-Si in the as-received condition and for GA-coated specimens in both the as-received and hot-stamped conditions. Figure 13 shows profiles for specimens in the as-received and hot-stamped conditions for Al-Si and GA specimens. It can be observed that both coating types produce similar dynamic resistance profiles, regarding the number of stages, but the features/stages in the profiles are sharper and more detectable for materials in the hot-stamped conditions due to the higher resistance and higher coating thickness in the hot-stamped

condition. For example, the coating removal stage is not visible in the profile for GA (AR) specimen due to the very small thickness of the coating (see Figure 3(a)), but is very visible in the hot-stamped condition of GA (HS). Thus, the model of Gedeon and Eager<sup>[9]</sup> for GA-coated steel is also generally applicable for Al-Si-coated steel except for the missing initial heating stage “0” which will be presented in greater detail in the next section.

### 3. Stage 0 of the dynamic resistance profile

The initial rise in resistance during RSW is due to heating effect as current begins to flow, causing voltage build-up, to attain the surface oxide film breakdown voltage<sup>[5,9,23]</sup> before fritting begins. It is for this reason that the *initial peak* dynamic resistance values (see, for example, Figure 14) are different from static resistance values (which are measured at room temperature). To



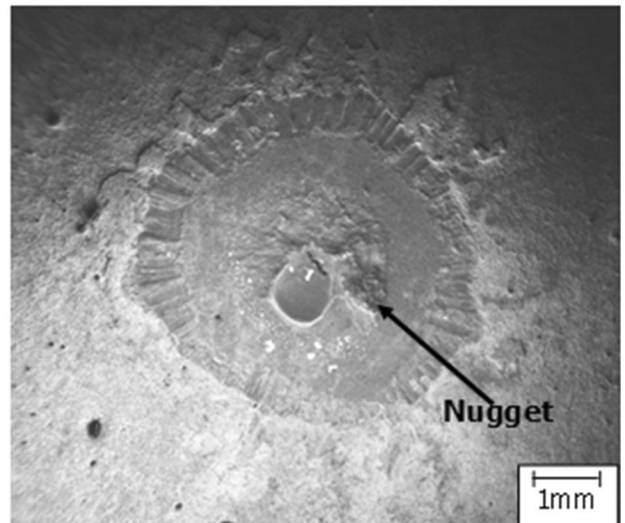
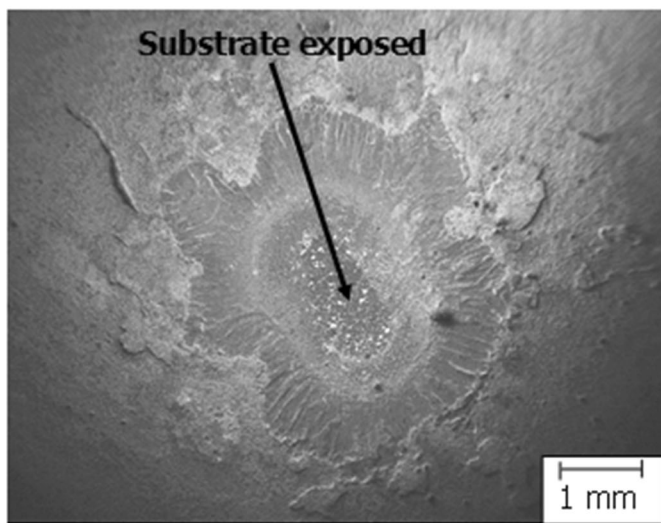
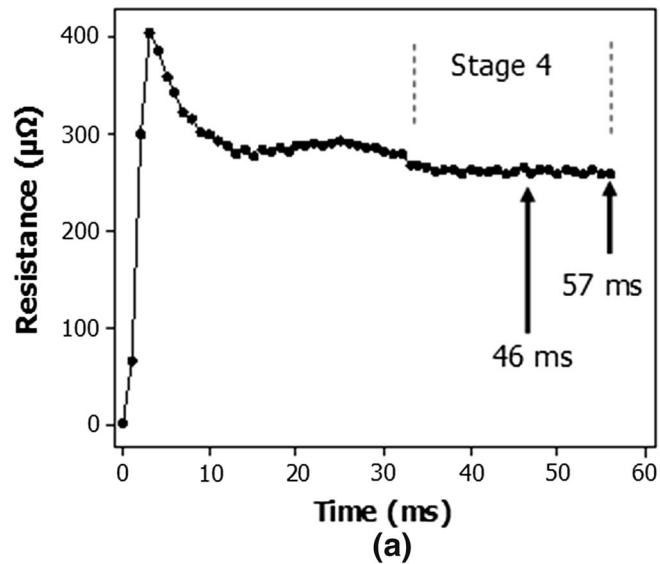


Fig. 11—(a) Dynamic resistance profile for Al-Si (HS) welded at 7.5 kA, showing up to stage 4 when heat is concentrated on the substrate; (b) microstructure of faying interface corresponding to 47 ms of welding showing a portion of the substrate steel after the coating has melted and been displaced; (c) microstructure of faying interface corresponding to a weld time of 57 ms showing nugget formation.

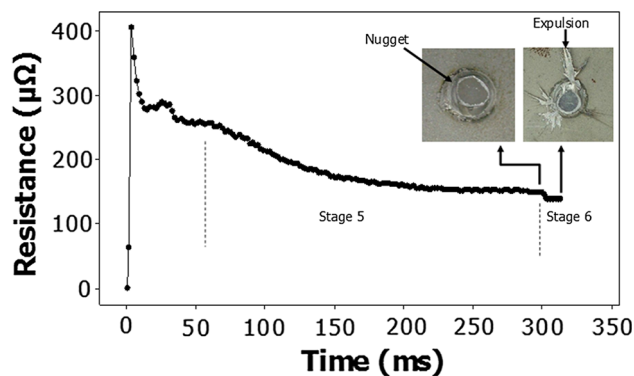


Fig. 12—Resistance profile for Al-Si (HS), 7.5 kA weld current showing up to stages 5 and 6 during growth of nugget (and expulsion when weld time is excessive).

substantiate the existence of this initial heating stage, welding was conducted on Al-Si and GA specimens using different welding currents to ensure different heating rates. It was observed that as the welding current increased, this initial peak resistance value decreased for two reasons: firstly, high current results in low resistance because of a constant film breakdown voltage; secondly, higher current results in higher heating rate, which softens and flattens the asperities faster, therefore causing the resistance to begin to drop from relatively lower values. This fact is reinforced by Figure 14 where it is shown for Al-Si (AR) and GA (AR) that as the welding current increased, the initial peak resistance decreased. The same is also true for hot-stamped specimens shown in Figure 15.

To further support this position, welding was carried out at 2.0 kA to reduce the heating rate so as to attain

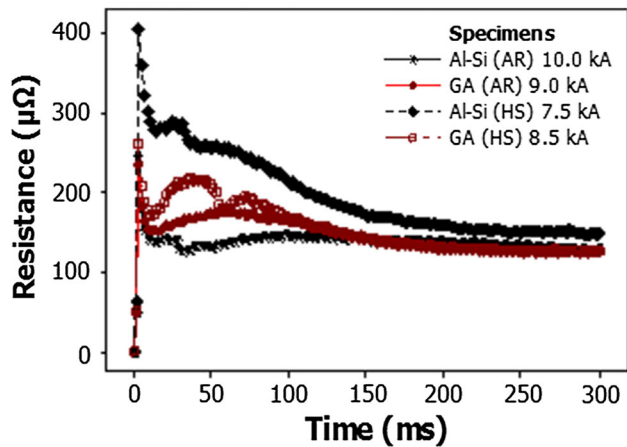


Fig. 13—Dynamic resistance profiles for the specimens and their welding currents.

much higher initial resistance value due to the delay in softening of asperities. The results are illustrated in Figure 16 which shows the first 50 ms of the dynamic resistance profiles for the as-received GA- and Al-Si-coated specimens. The peak resistance values are 523 and 755  $\mu\Omega$  for the GA- and Al-Si-coated specimens, respectively. These values were not attained using higher welding currents shown in Figure 14.

These analyses are particularly important and necessary for two reasons: Firstly, it establishes the reason why the initial peak value for dynamic resistance cannot be taken as the value for static resistance; initial dynamic resistance value is higher than the static resistance value for the as-received coated specimens (example of low-resistance situation) but lower than the static resistance value for hot-stamped coated specimens (examples of high-resistance situation). Secondly, the analyses establish the existence of a heating stage before stage 1 (surface film breakdown) of the model by Gedeon and Eager,<sup>[9]</sup> and thus help produce a more complete model for the dynamic resistance profile for coated steels during RSW. To conform with the earlier model by Gedeon and Eager,<sup>[9]</sup> this initial heating stage is referred to as “Stage zero” (*stage 0*). A summary of a generalized model for dynamic resistance profile for coated steel using mid-frequency direct current (MFDC) power supply is presented in Figure 17. However, the exact profile for any specimen depends on the parameters used during welding as well as the materials and coating morphology.

### C. Computation of Resistance Components

To compute the components of resistance during RSW, Eqs. [4] through [7] developed in the background Section I–A were employed. For evaluation of the faying interface resistance, RSW for the single sheet set-up (as shown in Figure 2) was carried out. Figure 18 shows the dynamic resistance profiles for three single sheets (S1, S2, and S3) and three double sheets (D1, D2, and D3) for the Al-Si and GA specimens. The three profiles shown for each of the single and double sheets is

meant to show consistency in their profiles. It was observed that the ends of stage 1 (first minimum point on dynamic resistance profile) for both the double and single sheet set-ups are coincident (See Figure 18 (a) through (d)). This makes it possible to carry out the evaluation at the common/coincident point, when the surface film has no influence and the set-up is still at room temperature. The mean differences between the resistances of the single and double sheets at the end of stage 1 are shown on each specimen set in Figure 18; these represent the mean values of  $R_{T2} - R_{T1}$  of Eq. [7].

At room temperature, the resistivity of Cu electrode is taken as  $1.69 \times 10^{-8} \Omega$ .<sup>[24]</sup> Considering the magnitude of the resistivity of Usibor ( $23.02 \times 10^{-8} \Omega\text{m}$  in the as-received condition) and Cu, and that the heat generated by the Cu electrode does not contribute to heating the joint since it is absorbed by the electrode cooling water, the contribution of Cu electrode to the total resistance and heat generation is reasonably negligible. The current path through the sheets is 2.4 mm (each sheet is 1.2 mm thick, and coating thickness is negligible). Using the area under 6.0-mm-diameter electrode, Eq. [4] ( $R_b = \rho \frac{L}{A}$ ) enables the computation of bulk resistance. Using Eq. [7], the values of  $R_{fa}$  were computed, and the computation of  $R_{e/s}$  was performed using either Eq. [5] or [6]. Figure 19 (error bars represent  $\pm 1$  standard deviation) shows the graphs of the computed values of the faying interface and electrode/sheet interface resistances at the beginning of welding. From Figure 19(a), it can be seen that the faying interface resistance for the hot-stamped specimens is higher than that for the as-received specimens. This is as expected since the surfaces are usually rougher after hot stamping. In the case of Al-Si, the coating is entirely transformed into new phases:  $\text{Fe}_2\text{Al}_5$  and  $\text{FeAl}$ .<sup>[14,16]</sup> The hardness of the  $\text{FeAl}$  phase is between 400 and 520 HV,<sup>[14,20]</sup> while the hardness of the  $\text{Fe}_2\text{Al}_5$  is between 900 and 1150 HV.<sup>[14]</sup> But the hardness of Al-Si coating in the as-received condition is between 62 and 68 HV.<sup>[25]</sup> Since the phases after hot stamping are much harder, Eq. [1] shows that the apparent contact area in the hot-stamped condition will be smaller, causing the contact resistance to increase. For the GA coating, during hot stamping at 1173 K (900 °C) the different phases no longer exist [beyond 1055 K (782 °C)] as shown in the Fe-Zn phase diagram (Figure 6), but the liquid phase and solid solution of Zn in  $\alpha$ -Fe exist. Thus, the slight increase in  $R_{fa}$  for the GA-coated steel after hot stamping is principally due to higher surface roughness. The numerical values from Figure 19(a) provide more insight into the RSW process. They indicate the relative magnitudes of current required for welding the specimens since nugget formation usually begins from this region. This is consistent with the work reported here, where 7.5 and 8.5 kA welding currents were required to produce full nugget sizes (5.9 mm) for hot-stamped Al-Si- and GA-coated sheets, while in the as-received conditions the welding currents of 10.0 and 9.0 kA were required to produce similar-sized nuggets for Al-Si- and GA-coated specimens, respectively. Also, because the values of faying interface resistance of the

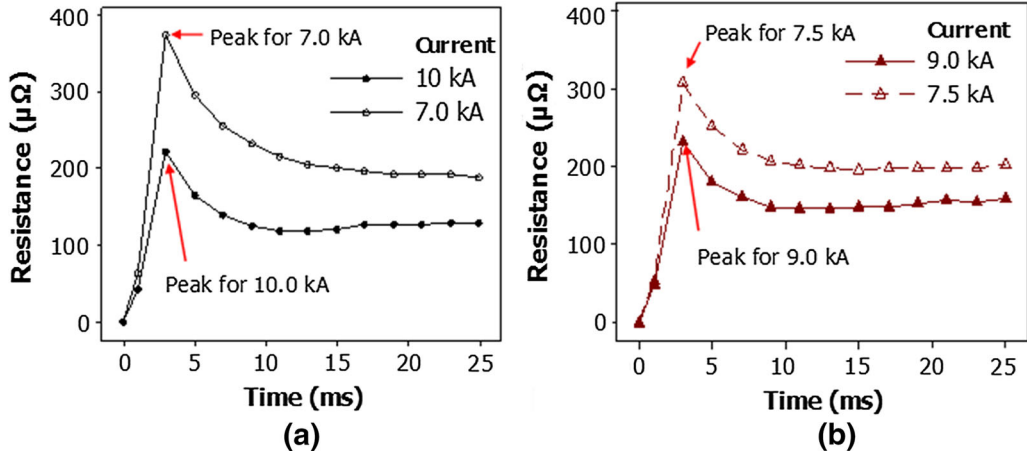


Fig. 14—Initial peak resistance variations with welding current for the as-received specimens: as the welding current increased, the initial peak resistance decreased for (a) Al-Si (AR) and (b) GA (AR).

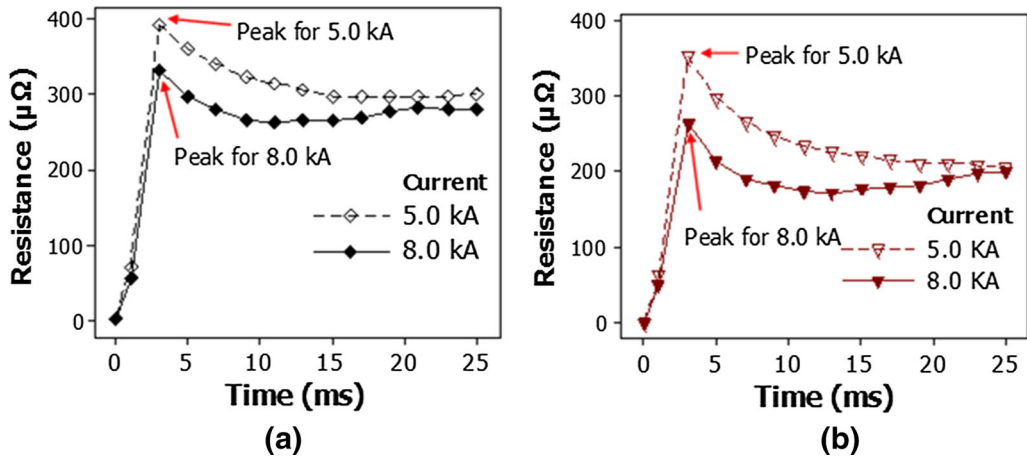


Fig. 15—Initial peak resistance variations with welding current for hot-stamped specimens: as the welding current increased, the initial peak resistance decreased for (a) Al-Si (HS) and (b) GA (HS).

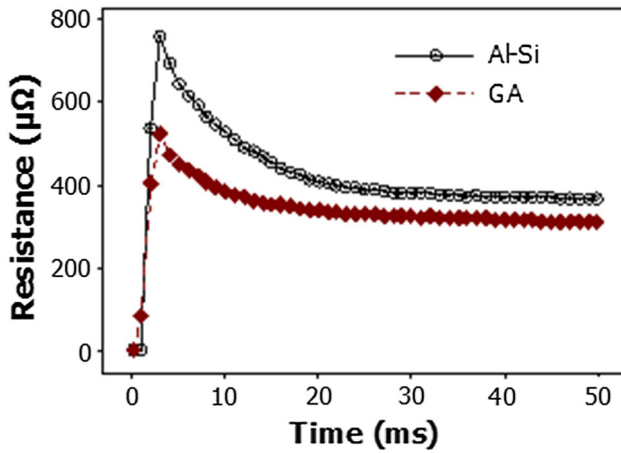


Fig. 16—Dynamic resistance profiles for the as-received Al-Si- and GA-coated specimens welded at 2.0 kA during the first 50 ms.

as-received and hot-stamped GA-coated materials are reasonably similar, their welding current requirements are also reasonably similar. Therefore, it is expected that

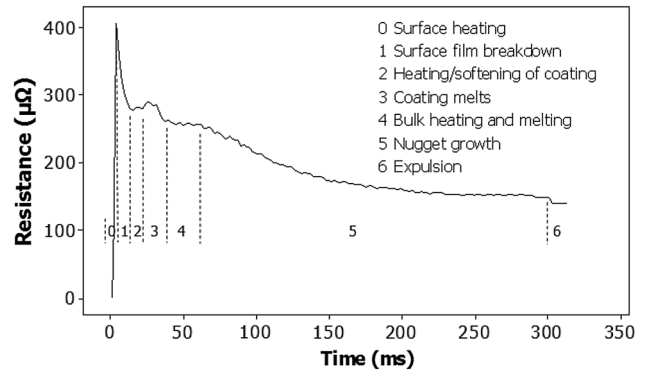


Fig. 17—Stages in generalized dynamic resistance profile for coated steels using MFDC power supply.

similar parameters can be used for welding the as-received and hot-stamped GA materials, whereas very different welding parameters are needed for the as-received and hot-stamped Al-Si-coated PHS. The dynamic resistance profiles for these welds are also shown in

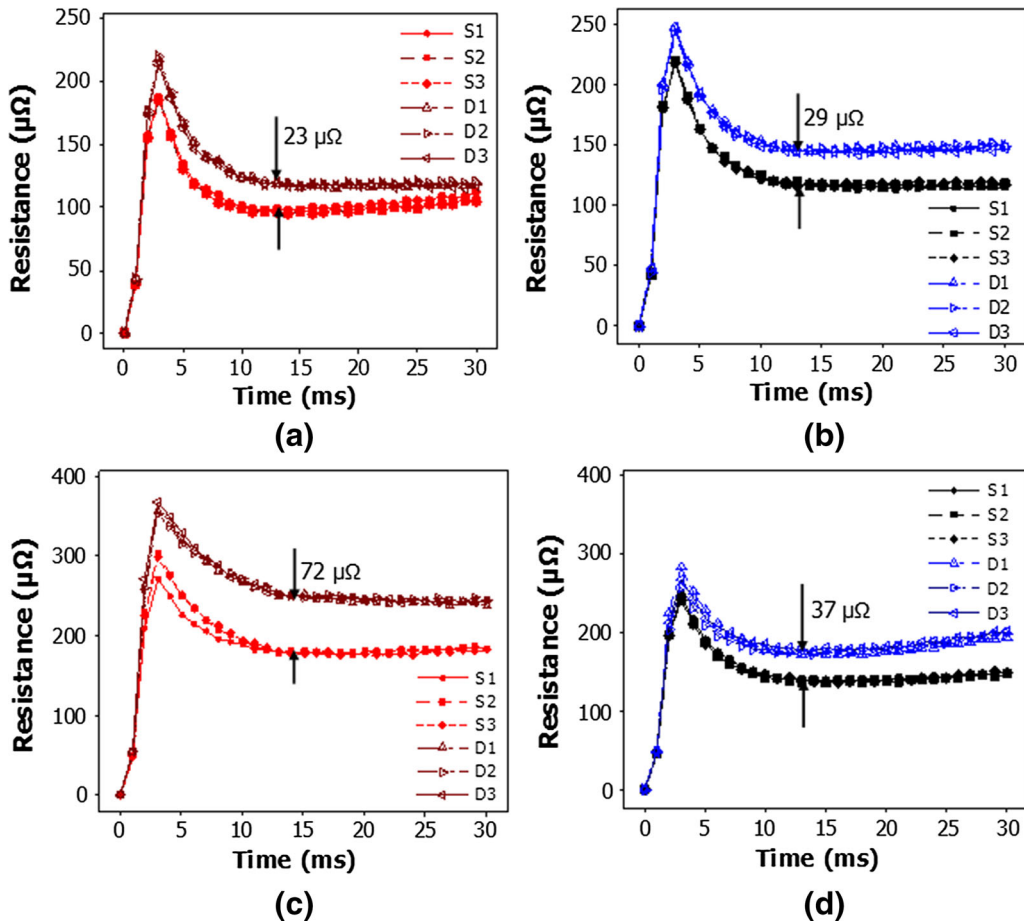


Fig. 18—Comparison of dynamic resistance profiles for single and double sheets during early stages of RSW process: (a) Al-Si (AR), (b) GA (AR), (c) Al-Si (HS), and (d) GA (HS). S1, S2, and S3 are profiles for single sheets; D1, D2, and D3 are profiles for double sheets.

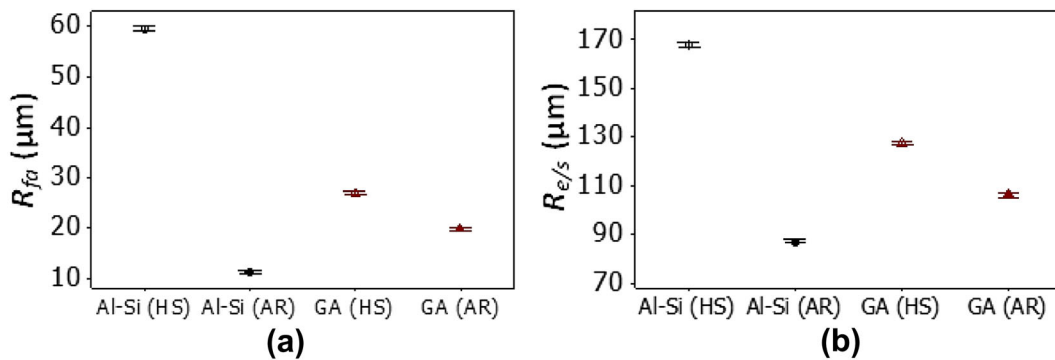


Fig. 19—Components of resistance for the coated specimens (at 95 pct confidence interval): (a) faying interface resistance and (b) electrode/sheet interface resistance.

Figure 13, where it can be seen that the emergence of the stages is consistent with the trend in  $R_{fa}$ : for example, stage 4 (beginning of nugget formation) occurred in the shortest time for the Al-Si (HS) specimen and the longest time for the Al-Si (AR) specimen.

Figure 19(b) shows the trend in  $R_{e/s}$ . The distribution follows a similar pattern to that of  $R_{fa}$ : hot-stamped materials having higher  $R_{e/s}$  values and Al-Si (HS) having much higher values than all the others.

Comparing Figures 19(a) and (b), it can be seen that  $e/s$  interface resistance values are much higher than the faying interface resistances. This suggests, according to Joule heating effect, that more heat should be generated at the  $e/s$  interface region, which should cause melting to begin at the  $e/s$  interface. However, due to heat loss because of exposure of the  $e/s$  interface to atmosphere and cooling from the electrode caps, the temperature at the  $e/s$  interface will be much lower than the faying

**Table II. Percentages of Resistance Components at the Onset of RSW Process for Al-Si- and GA-Coated Hot-Stamping Steel**

	Al-Si		GA	
	AR	HS	AR	HS
$2R_b$ ( $\mu\Omega$ )	16.7	8.1	13.5	11.5
$R_{fa}$ ( $\mu\Omega$ )	11.3	24.8	13.3	15.2
$2R_{e/s}$ ( $\mu\Omega$ )	72.0	67.1	73.2	73.3

interface temperature. Consequently, fusion will normally take place at the faying interface. Figure 19(b) may also be useful for predicting the relative rate of electrode degradation since the rate at which degradation (by softening and deformation) occurs depends on the maximum temperature attained at the e/s interface.<sup>[26]</sup> Thus, with the Al-Si (HS) specimen having the highest  $R_{e/s}$ , during welding of Al-Si (HS), electrode tip heating, softening, and mushrooming are expected to most likely occur at a higher rate. This relatively high  $R_{(e/s)}$  is also an indicator of likelihood of degradation of the electrodes which may occur as a consequence of segregation of phases due to high heating rate at the electrode interface. However, this expectation is subject to further investigation. Table II shows, in summary, the percentages of the components of these resistances.

#### IV. SUMMARY AND CONCLUSION

Dynamic resistance profiles have been used to study spot welding process of Al-Si- and GA-coated steels in the as-received and hot-stamped conditions and the conclusions are summarized as follows:

1. The dynamic resistance profile for Al-Si- and GA-coated Usibor® are similar, and six (or seven if expulsion is included) distinct stages have been identified in the generalized profile. The profiles are similar for both the as-received and hot-stamped specimens, except that the features for each stage are more pronounced in the hot-stamped condition than in the as-received condition.
2. The existence of an initial heating stage prior to fritting/surface film breakdown was established. This makes the resistance values obtained from static measurement significantly different from the initial peaks obtained at the beginning of the dynamic resistance profile. It explains why these initial peaks in dynamic resistance profile depend on the welding current, and also why the initial peak values of dynamic resistance are lower than the static resistance values for hot-stamped materials but are higher than the static resistance values for materials in the as-received condition.
3. A method was developed for computing the magnitude of resistance associated with key sections in the set-up for RSW by the application of dynamic resistance profiles. It was shown that in all cases the electrode/sheet interface resistance is significantly

higher than the faying interface resistance at the beginning of RSW.

4. The value of the faying interface resistance could be useful for comparing welding current requirement associated with different coatings since the trend in magnitude of the faying interface resistance correlates directly with the magnitude of the current required for nugget formation for the coated specimens. Likewise, the e/s interface resistance could be useful for predicting or comparing the rate of electrode degradation during RSW since the factor that causes electrode tip degradation directly correlates with temperature.

#### ACKNOWLEDGMENTS

The authors are thankful to ArcelorMittal Dofasco Inc., Hamilton, Canada, for the supply of materials for this work and to Professor Michael Worswick of the Department of Mechanical and Mechatronics Engineering, University of Waterloo, Ontario, Canada, for the use of his hot-stamping facility. Financial support from the Natural Science and Engineering Research Council of Canada (NSERC) is greatly acknowledged.

#### REFERENCES

1. X. Hu, G. Zou, S.J. Dong, M.Y. Lee, J.P. Jung, and Y. Zhou: *Mater. Trans.*, 2010, vol. 51 (12), pp. 2236–42.
2. W. Tan, Y. Zhou, and H.W. Kerr: *Metall. Mater. Trans. A*, 2002, vol. 33A, pp. 2667–76.
3. W.F. Savage, E.F. Nippes, and F.A. Wassell: *Weld. Res. Suppl.*, 1978, vol. 43, pp. 43s–50s.
4. S.A. Gedeon, C.D. Sorensen, K.T. Ulrich, and T.W. Eagar: *Weld. Res. Suppl.*, 1987, vol. 8, pp. 378s–385s.
5. S. Bhattacharya and D.R. Andrews: *Weld Metal Fabr.*, 1974, vol. 42, pp. 296–301.
6. G. Banerjee, T.K. Pal, N. Bandyopadhyay, and D. Bhattacharjee: *Corros. Eng. Sci. Technol.*, 2011, vol. 46 (1), pp. 64–69.
7. N. Harlin, T.B. Jones, and J.D. Parker: *J. Mater. Process. Technol.*, 2003, vols. 143–144, pp. 448–53.
8. N.A. Freytag: *Weld. J.*, 1965, vol. 44, pp. 145–56.
9. S.A. Gedeon and T.W. Eagar: *Metall. Mater. Trans. B*, 1986, vol. 17B, pp. 887–901.
10. C. Ma, S.D. Bhole, D.L. Chen, A. Lee, E. Biro, and G. Boudreau: *Sci. Technol. Weld. Join.*, 2006, vol. 11 (4), pp. 480–87.
11. R. Holm: *Electric Contacts Theory and Applications*, 4th ed., Springer, Berlin, 1967, p. 2.
12. D.W. Dickinson, J.E. Franklin, and A. Stanya: *Weld. Res. Suppl.*, 1980, vol. 59 (6), pp. 170s–76s.
13. A.R. Marder: *Prog. Mater. Sci.*, 2000, vol. 45, pp. 191–271.
14. M. Windmann, A. Röttger, and W. Theisen: *Surf. Coat. Technol.*, 2014, vol. 246, pp. 17–25.
15. S.J. Grauer, E.J.F.R. Caron, N.L. Chester, M.A. Wells, and K.J. Daun: *J. Mater. Process. Technol.*, 2015, vol. 216, pp. 89–94.
16. I.I. Danzo, Y. Houbaert, and K. Verbeken: *Surf. Coat. Technol.*, 2014, vol. 251, pp. 15–20.
17. S. Kobayashi and T. Yakou: *Mater. Sci. Eng. A*, 2002, vol. 338, pp. 44–53.
18. R. Brandt and G. Neuer: *Int. J. Thermophys.*, 2007, vol. 28 (5), pp. 1429–46.
19. S. Jazbec, P. Kozelj, S. Vrtnik, Z. Jaglicic, P. Popcevic, J. Ivkov, D. Stanic, A. Smontara, M. Feuerbacher, and J. Dolinsek: *Phys. Rev. B*, 2012, vol. 86 (6), pp. 1–8.
20. M.R. Hajaligol, S.C. Deevi, V.K. Sikka, and C.R. Scorey: *Mater. Sci. Eng. A*, 1998, vol. 258, pp. 249–57.

21. A.C. Lilly, S.C. Deevi, and Z.P. Gibbs: *Mater. Sci. Eng. A*, 1998, vol. 258, pp. 42–49.
22. Y.B. Pithawalla, M.S. El Shall, and S.C. Deevi: *Intermetallics*, 2000, vol. 8, pp. 1225–31.
23. W. Tan, Y. Zhou, H.W. Kerr, and S. Lawson: *J. Phys. D*, 2004, vol. 37, pp. 1998–2008.
24. A. Tsalif: *Combined Properties of Conductors*, Elsevier Scientific, New York, 1981.
25. H. Elzanaty: *Int. J. Res. Eng. Technol.*, 2014, vol. 2 (7), pp. 49–54.
26. N.T. Williams and J.D. Parker: *Int. Mater. Rev.*, 2004, vol. 49 (2), pp. 77–108.